Elevated Temperature Anodized Nb_2O_5: A Photoanode Material with Exceptionally Large Photoconversion Efficiencies

Jian Zhen Ou,[†,*] Rozina A. Rani,[†] Moon-Ho Ham,[‡,§] Matthew R. Field,[⊥] Yuan Zhang,[†] Haidong Zheng,[†] Peter Reece,[∥] Serge Zhuiykov,[¶] Sharath Sriram,[†] Madhu Bhaskaran,[†] Richard B. Kaner,[#] and Kourosh Kalantar-zadeh[†,*]

[†]School of Electrical and Computer Engineering, RMIT University, Melbourne, VIC, Australia, [‡]Department of Chemical Engineering, Massachusetts Institute of Technology, Cambridge, Massachusetts 02139, United States, [§]School of Materials Science and Engineering, Gwangju Institute of Science and Technology, Gwangju, Korea, [⊥]School of Applied Science, RMIT University, Melbourne, VIC, Australia, [∥]School of Physics, University of New South Wales, Sydney, New South Wales, Australia, [¶]Materials Science and Engineering Division, CSIRO, Highett, Victoria, Australia, and [#]Department of Materials Science and Engineering, University of California, Los Angeles, California 90095, United States

ABSTRACT

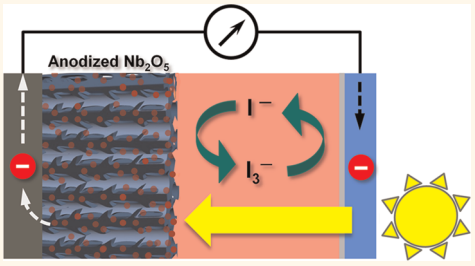

Here, we demonstrate that niobium pentoxide (Nb_2O_5) is an ideal candidate for increasing the efficiencies of dye-sensitized solar cells (DSSCs). The key lies in developing a Nb_2O_5 crisscross nanoporous network, using our unique elevated temperature anodization process. For the same thicknesses of ~4 μm, the DSSC based on the Nb_2O_5 layer has a significantly higher efficiency (~4.1%) when compared to that which incorporates a titanium dioxide nanotubular layer (~2.7%). This is the highest efficiency among all of the reported photoanodes for such a thickness when utilizing back-side illumination. We ascribe this to a combination of reduced electron scattering, greater surface area, wider band gap, and higher conduction band edge, as well as longer effective electron lifetimes.

KEYWORDS: dye-sensitized solar cell · Nb_2O_5 · nanoporous network · TiO_2 · anodization

Ordered titanium dioxide (TiO_2) nanotube arrays in dye-sensitized solar cells (DSSCs), which can potentially increase the electron diffusion length, have shown enhancements in the efficiencies of both charge collection and light harvesting.[1−3] However, similar to other alternative approaches,[4−7] the power conversion efficiency of the TiO_2 nanotube arrays still remains lower than that of nanoparticle films.[8−10] It has been suggested that this is due to their reduced available surface sites for dye loading and the possible existence of exciton-like trap states.[11] In searching for a better solution for developing highly efficient DSSCs, niobium pentoxide (Nb_2O_5) could be a more suitable candidate than TiO_2 and other semiconductors[12−14] in view of its wider band gap and higher conduction band edge (presented in Figure 1),[15,16] comparable electron injection efficiency,[17,18] as well as better chemical stability.[19] While Nb_2O_5 nanoparticles,[16] nanobelts,[20] and nanofiber networks[15] have been studied for the development of DSSCs, their photocurrents and photoconversion efficiencies have not reached those of TiO_2-based DSSCs due to the reduction in their dye-loading sites.[15,16,20] It has been suggested that the large unit cell dimension of orthorhombic Nb_2O_5, in comparison to anatase TiO_2, makes it a challenging task to obtain the optimum Nb_2O_5 morphology for DSSC applications.[19] The original discovery of a vertically positioned Nb_2O_5 nanoporous layer gave hope for solving this problem, but the limited thickness of the layer (<500 nm) made it unrealistic as a candidate for DSSCs.[21,22] Here, we report a critical breakthrough with the synthesis of Nb_2O_5 crisscross nanoporous networks with thicknesses of up to ~4 μm *via* a novel electrochemical anodization method carried outat elevated temperatures. The elevated temperature condition was applied based on

* Address correspondence to j.ou@student.rmit.edu.au, kourosh.kalantar@rmit.edu.au.

Received for review January 27, 2012 and accepted April 18, 2012.

Published online April 18, 2012
10.1021/nn300408p

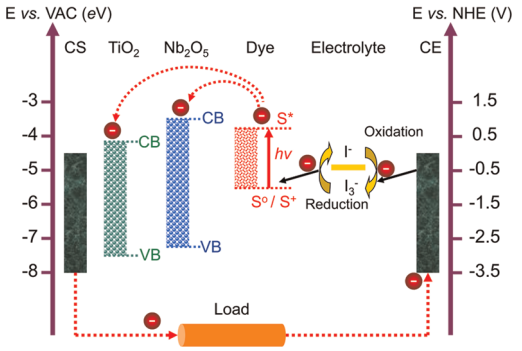

Figure 1. Energy state diagram of Nb_2O_5 and TiO_2-based DSSCs featuring their operation principle, in which CS, CE, CB, VB, VAC, and NHE stand for conductive substrate, counter electrode, conduction band, valence band, vacuum, and normal hydrogen electrode, respectively.

the hypothesis that it increases the ion diffusion rate during the anodization process, hence increasing the anodized film thickness. DSSCs with photoanodes based on these structures have been fabricated and demonstrate superior performances in comparison to their TiO_2 counterparts.

RESULTS AND DISCUSSION

In the anodization process of niobium (Nb), two factors have been suggested to be the main causes for preventing the formation of porous layers thicker than 500 nm.[21,22] The first is the high chemical dissolution rate of the porous layer caused by fluorine ions in the electrolytes. The second is the formation of a thick barrier layer on the bottom of the pores, which inhibits further ion diffusion and growth of the porous layer. In order to increase the layer thickness to several micrometers, we first utilized ethylene glycol instead of water as the solvent, which helps reduce the chemical dissolution effect on the porous layer.[23] Second, we increased the electrolyte temperature to 50 °C to enhance the diffusion rate of the ions, thereby enhancing the growth rate of the porous layer.[24−26] The selection of electrolyte temperature is another important parameter that requires optimization. In this study, we found that the chemical dissolution effect on the porous layer is greatly increased even in the presence of ethylene glycol for temperatures above 50 °C, while the growth rate of the porous layer drops rapidly at temperatures below 50 °C. A detailed description of the anodization process is provided in the Methods section.

The scanning electron microscopy (SEM) image in Figure 2a depicts the surface morphology of the as-anodized niobium oxide layer. A highly organized pore distribution is observed with nanosized pores ranging from 30 to 50 nm. The side walls are around 10 to 20 nm thick. The bottom of the anodized layer (Figure 2c) consists of uniform and packed pseudo-semispheres

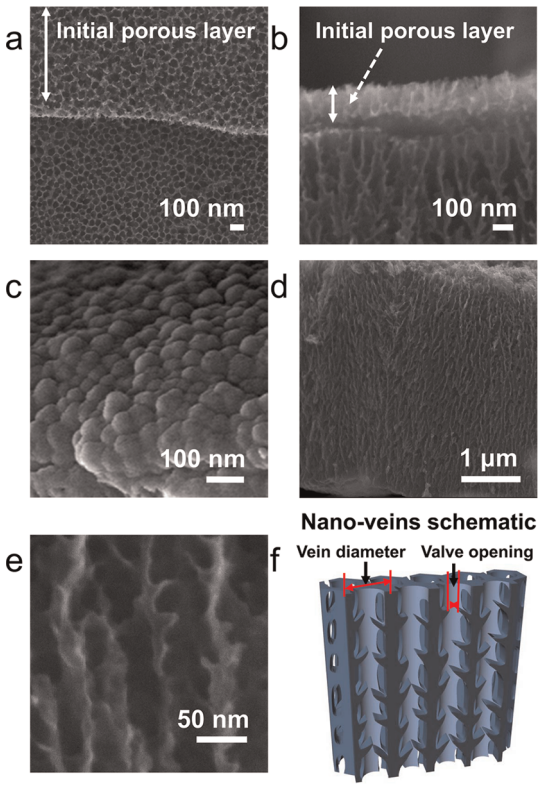

Figure 2. SEM images of a Nb_2O_5 nanoporous network. (a) Top view of the nanoporous network. (b) Cross-sectional view of the top of the nanoporous network. (c) Bottom view of the nanoporous network. (d) Cross-sectional view of the whole nanoporous network. (e) Higher magnification SEM images of cross-sectional view of the nanoporous network. (f) Three-dimensional schematic of the cross-sectional view of the nanoporous network.

with a diameter of approximately 50 nm, which is close to that of the pore dimensions. Similar to the anodization of Ti and Al, the formation of these pseudo-semispheres could result from the mechanical stress induced by the effect of the niobium oxide volume expansion.[27] Figure 2d depicts a ~4 μm thick porous layer which is formed after 2 h of anodization with a stratified structure consisting of couple different regions. By zooming in on the cross-sectional image, a ~100−200 nm thick porous layer can be seen on top (Figure 2b). The top morphologies of both upper and underneath layers are almost similar, except that the side walls of the upper layer are thinner and the pores are less ordered, probably due to the chemical dissolution effect (Figure 2a). This upper layer, with similar morphology and thickness to previously reported anodized niobium oxide structures, could be the initial porous layer formed at the beginning of the anodization process. The absence of a barrier layer underneath this initial layer provides further evidence for an enhancement of the rate of ion diffusion created by our unique anodization method at an elevated temperature. The main thick (underneath) layer appears to be made of continuous and highly packed vein-like nanostructured networks (more cross-sectional SEM

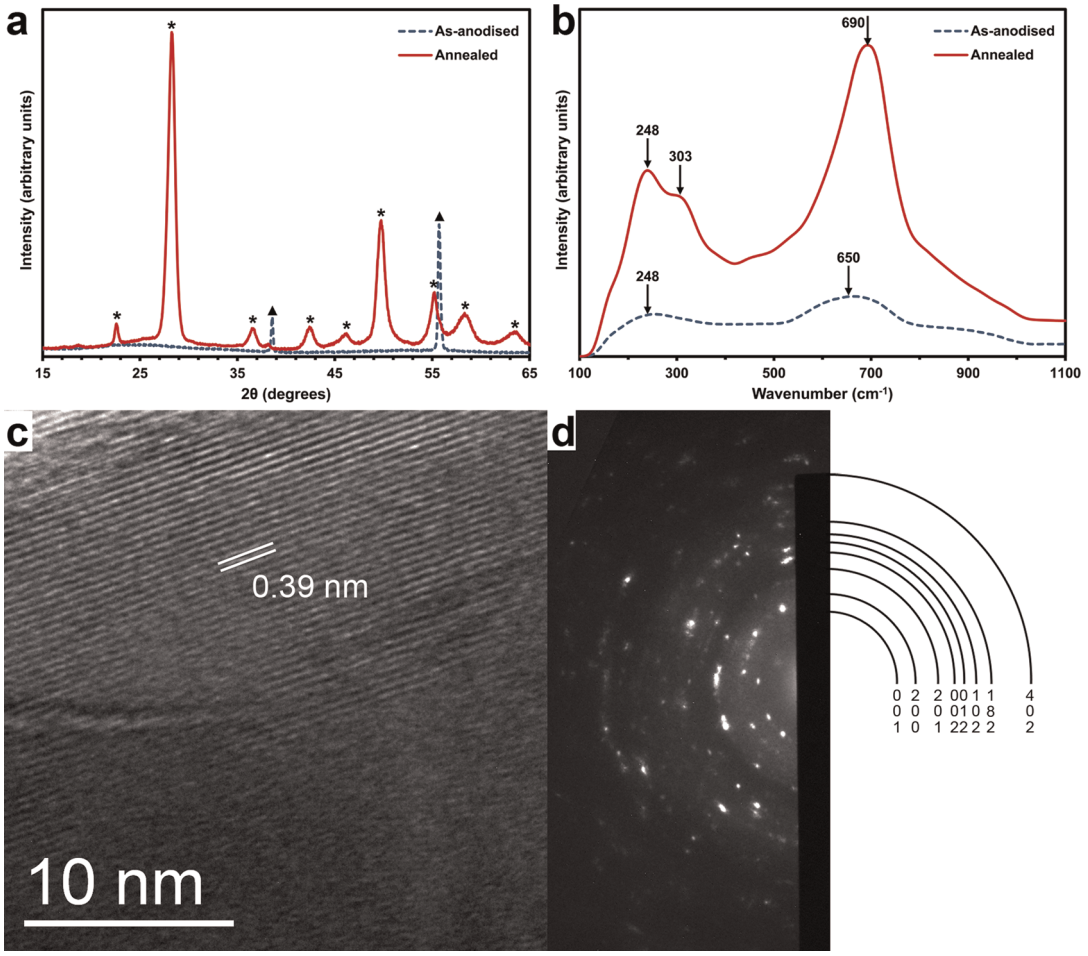

Figure 3. Crystal structure of a niobium oxide nanoporous network before and after annealing. (a) Dashed blue line is the XRD pattern of an as-anodized niobium oxide nanoporous network under the same fabrication conditions as Figure 2, and the red line is the XRD pattern of the network after annealing at 440 °C in air for 20 min. Orthorhombic Nb_2O_5 (ICDD 27-1003) is indicated with *, while Nb metal (ICDD 35-0789) is indicated with ▲. (b) Corresponding Raman spectra of the as-anodized (dashed blue line) and post-annealed network (red line). (c) HRTEM image of one of the nanoporous areas for Nb_2O_5 nanoporous networks after annealing. The 0.39 nm spacings with no cross-hatches indicate that the orthorhombic phase is present. (d) Corresponding selected area diffraction pattern indexed to the Nb_2O_5 orthorhombic phase.

images are provided in Figure S1 in the Supporting Information). There are also occasional lateral openings interconnecting them (Figure S1b,f). The "nanoveins" have internal diameters ranging from 30 to 60 nm, while the diameters of the "nanovein valves" are typically reduced by up to 80% of the veins' original internal diameters (Figure 2e,f). The valves are possibly the residual growths from the internal walls due to the chemical dissolution caused by fluorine ions in the electrolytes. However, two possible chemical dissolution processes, which are field-assisted and localized (random) dissolutions, are generally suggested to contribute to the metal oxide anodized nanoporous structure formation.[28] In order to find out the dominant mechanism for the formation of these Nb_2O_5 nanoveins, we weakened the electrical field by reducing the anodic voltage from 10 to 5 V during the anodization process, while keeping the fluoride concentration and the rest of the process conditions the same. From the SEM images shown in Figure S2, it can be observed that the density of nanoveins was dramatically reduced. We hence conclude that the formation of these nanoveins is mainly due to the field-assisted chemical dissolution.

From the cross-sectional transmission electron microscopy (TEM) image shown in Figure S3, this criss-cross nanoporous network can provide excellent directional and continuous pathways for electron transfer in addition to enhanced surface area. This potentially reduces the electron scattering that has commonly been seen in a system made of only nanoparticles, hence fulfilling the prerequisites for developing highly efficient DSSCs.[29]

The growth of the nanoporous network is very efficient with a growth rate of ~2 μm/h for the first 2 h (Figures S4 and S5). However, the organized porous surface is partially destroyed, due to excessive chemical dissolution when the anodization duration exceeds 2 h. In addition, saturation occurs and the thickness does not increase further after 3 h of anodization. The surface morphology and thickness of the nanoporous

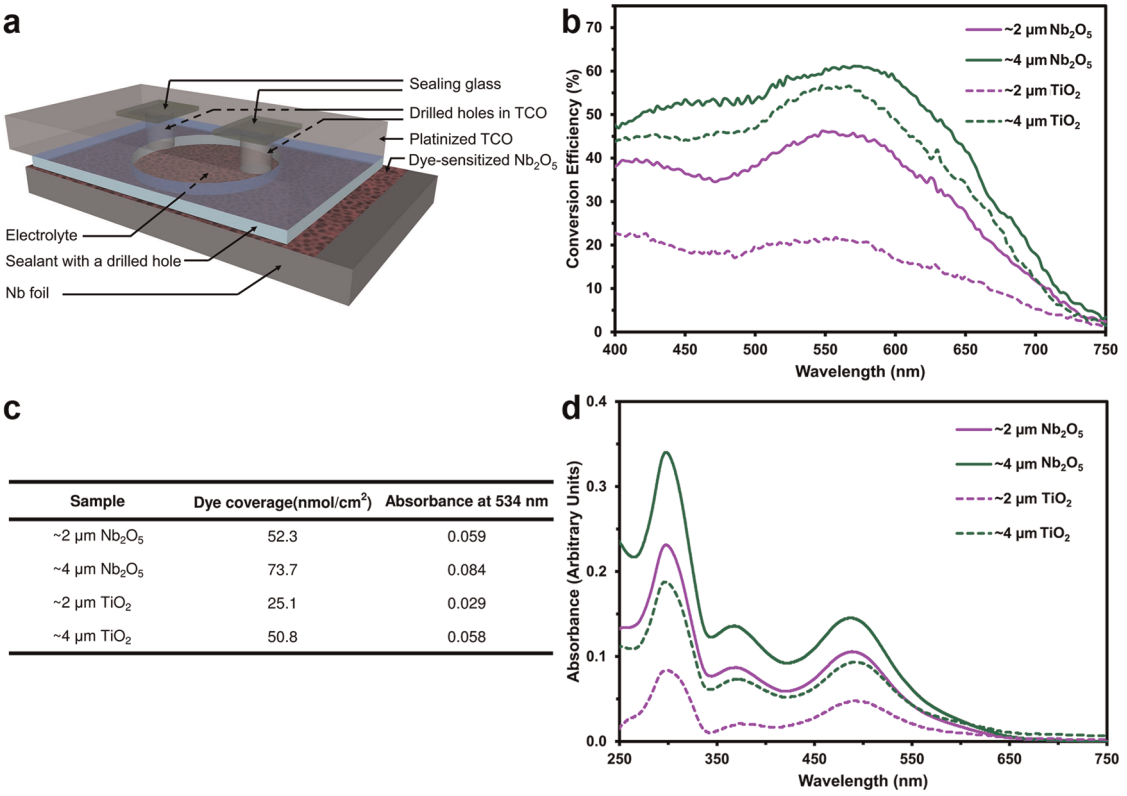

c

Sample	Dye coverage(nmol/cm^2)	Absorbance at 534 nm
~2 μm Nb_2O_5	52.3	0.059
~4 μm Nb_2O_5	73.7	0.084
~2 μm TiO_2	25.1	0.029
~4 μm TiO_2	50.8	0.058

Figure 4. Characteristics of the DSSCs fabricated using crystalline Nb_2O_5 nanoporous networks and anatase TiO_2 nanotube arrays. (a) Configuration of the DSSC fabricated incorporating the Nb_2O_5 nanoporous network. (b) IPCE spectra of DSSCs fabricated using Nb_2O_5 nanoporous networks and TiO_2 nanotube arrays of various thicknesses. IPCE was calculated using the relation IPCE % = 100$hcj(\lambda)/e\lambda P(\lambda)$, where h denotes the Planck constant, c the velocity of light, e the electron charge, λ the wavelength, $j(\lambda)$ the photocurrent density at λ, and $P(\lambda)$ the power density of light at λ. (c) Table of dye coverage detail of the Nb_2O_5 nanoporous networks and TiO_2 nanotube arrays. N3 dye attached on Nb_2O_5 nanoporous networks and TiO_2 nanotube arrays was desorbed by immersing the samples into a 10 mM KOH solution. The concentration of the desorbed dye determined by UV−vis spectroscopy was used to calculate the dye coverage in the samples. (d) UV−vis absorption spectra of N3 dye desorbed from Nb_2O_5 nanoporous networks and TiO_2 nanotube arrays of various thicknesses.

network can also be controlled by varying the fluoride content, the applied voltage, the water content, and the temperature. Details are provided in the Supporting Information.

From the XRD patterns (Figure 3a), the as-anodized nanoporous network appears to be amorphous and only niobium peaks are present in the diffractogram. Annealing of the porous network results in crystallization into a Nb_2O_5 orthorhombic structure (ICDD 27-1003, a = 6.168, b = 29.312, and c = 3.936 Å) with diffraction peaks at 28.3, 49.7, 55.1, 58, and 63.1° (more detailed analysis of XRD patterns are provided in the Supporting Information). The Raman spectra (Figure 3b) confirm the results obtained from the XRD measurements. For the as-anodized layer, a broad peak centered at 650 cm^{-1} represents the symmetric stretching mode ν (O−Nb−O) of amorphous niobium oxide.[30] Another weak peak at 242 cm^{-1} can be assigned to bending modes of Nb−O−Nb linkages. The Raman peaks become more prominent after annealing. In addition, there is a peak shift from 650 to 690 cm^{-1}, and a new peak appears at 303 cm^{-1}, both indicative of the orthorhombic nature of the annealed nanoporous network. According to theory, the orthorhombic and hexagonal (some literature states it as "pseudo-hexagonal") Nb_2O_5 structures both have very similar atomic structures.[31] High-resolution transmission electron microscopy (HRTEM) was utilized to further identify the crystal structure of this nanoporous network. Figure 3c shows the HRTEM image of the Nb_2O_5 nanoporous network in which parallel lattice fringes with spacings of 0.39 nm have been observed. This spacing has been seen previously by Weissman *et al.*,[31] who characterized Nb_2O_5 structures through a thorough TEM and *ab initio* investigation and observed this spacing to be indicative of the orthorhombic phase. Figure 3d shows a selected area diffraction (SAD) pattern of the Nb_2O_5 structure, which has been indexed to the orthorhombic phase.

The DSSCs based on ~2 and ~4 μm thick crystalline Nb_2O_5 nanoporous networks were assembled using a conventional configuration (Figure 4a).[32] The incident photon-to-electron conversion efficiency (IPCE) spectra of these DSSCs are shown in Figure 4b (pictures of samples after dye loading are provided in the Supporting Information) in comparison to anatase TiO_2 nanotube arrays with similar thicknesses as a benchmark (fabrication details are found in the Supporting

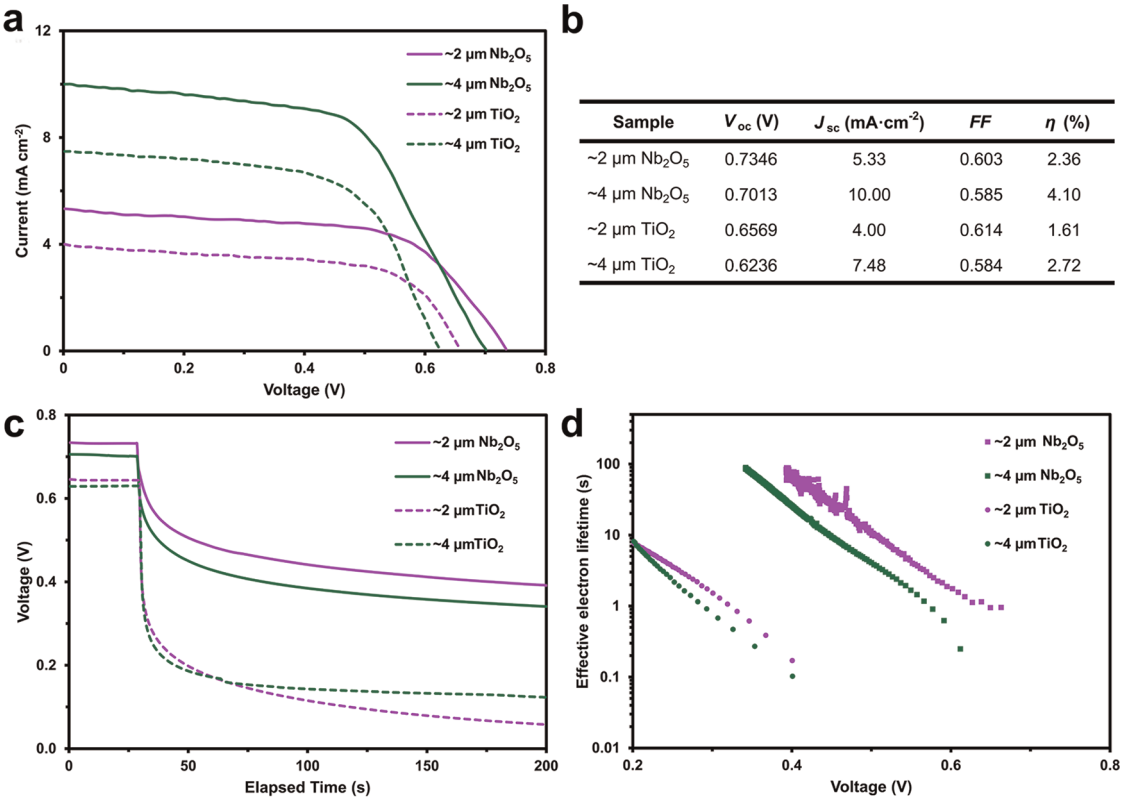

b

Sample	V_{oc} (V)	J_{sc} (mA·cm^{-2})	*FF*	η (%)
~2 μm Nb_2O_5	0.7346	5.33	0.603	2.36
~4 μm Nb_2O_5	0.7013	10.00	0.585	4.10
~2 μm TiO_2	0.6569	4.00	0.614	1.61
~4 μm TiO_2	0.6236	7.48	0.584	2.72

Figure 5. Performances of the DSSCs fabricated using crystalline Nb_2O_5 nanoporous networks and anatase TiO_2 nanotube arrays. (a) Current−voltage characteristics of DSSCs fabricated using Nb_2O_5 nanoporous networks and TiO_2 nanotube arrays of various thicknesses under the testing condition of Sun AM 1.5 (100 mW cm^{-2}). (b) Table of power conversion efficiencies of the Nb_2O_5 nanoporous networks and TiO_2 nanotube arrays. The efficiency was calculated using the relation $\eta = J_{SC}V_{OC}FF/P_t$, where J_{SC} is the short circuit current density, V_{OC} the open circuit voltage, FF the fill factor, and P_t the incident power density (100 mW cm^{-2}). (c) Photovoltage decay measurements of DSSCs fabricated using Nb_2O_5 nanoporous networks and TiO_2 nanotube arrays of various thicknesses. (d) Effective electron lifetime determined by open circuit voltage decay for DSSCs fabricated using Nb_2O_5 nanoporous networks and TiO_2 nanotube arrays of various thicknesses. The effective electron lifetime is determined using the relation $\tau_n = -k_BT[dV_{OC}/dt]^{-1}/e$, where k_BT is the thermal energy, dV_{OC}/dt is the derivative of open circuit voltage transient, and e is the positive elementary charge.

Information). The IPCE spectrum of the dye-loaded 4 μm thick Nb_2O_5 nanoporous network indicates two broad peaks in a wide wavelength range (400−750 nm). The center of the first peak is at 450 nm with a peak magnitude of 52.4%, while the other is at 575 nm with a 61.1% conversion efficiency. Significant conversion efficiencies can also be observed for wavelengths up to 750 nm. These impressive results are far superior to any other reported Nb_2O_5-based DSSCs that we are aware of and approximately 20% higher than that of TiO_2 nanotube arrays with a similar thickness. This enhancement becomes even more obvious for the 2 μm thick Nb_2O_5 nanoporous network, which surprisingly shows an almost 100% improvement when compared with that of a TiO_2 nanotube array. We believe that this noteworthy improvement of the conversion efficiency could be primarily due to the enhanced surface area of the Nb_2O_5 nanoporous networks. The 2 and 4 μm thick Nb_2O_5 nanoporous networks have a greater surface area by factors of 100 and 45%, respectively, in comparison to the equivalent TiO_2 nanotube arrays according to the dye coverage characterization presented in Figure 4c,d.

The current−voltage characteristics of these DSSCs are shown in Figure 5a,b. The DSSC with a ~4 μm thick Nb_2O_5 nanoporous network yields a power conversion efficiency of 4.1%. In comparison, a TiO_2 nanotube array based DSSC with similar thickness has an efficiency of only 2.7%, which is 51% below that of Nb_2O_5. Similarly, there is a 47% improvement in power conversion efficiency for a Nb_2O_5 nanoporous network when compared to a TiO_2 nanotube array when both thicknesses are reduced to ~2 μm. Note that the presence of a higher open circuit voltage V_{OC} for Nb_2O_5 when compared to TiO_2 is a commonly reported characteristic.[15,16,20] This is mainly due to wider band gap (~0.29 eV wider) and higher conduction band edge energy (as shown in Figure 1) of Nb_2O_5, as V_{OC} is proportional to the difference between the Fermi level of the Nb_2O_5 (or TiO_2) electrode and the electrochemical potential of the redox couple.[33]

In addition to the increase in open circuit voltage, the significant improvement in the short circuit photocurrent density J_{SC} may be due to a larger amount of loaded dye and also possibly less dye agglomerates formed on the oxide surfaces due to the better

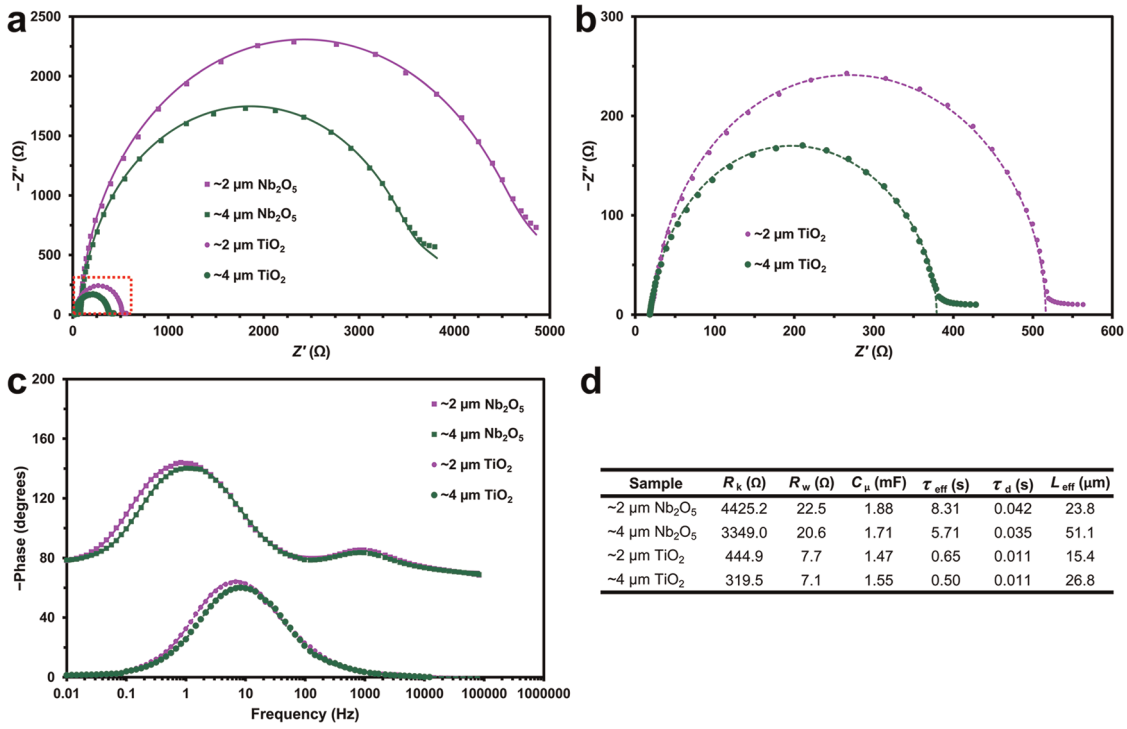

Sample	R_k (Ω)	R_w (Ω)	C_μ (mF)	τ_{eff} (s)	τ_d (s)	L_{eff} (μm)
~2 μm Nb_2O_5	4425.2	22.5	1.88	8.31	0.042	23.8
~4 μm Nb_2O_5	3349.0	20.6	1.71	5.71	0.035	51.1
~2 μm TiO_2	444.9	7.7	1.47	0.65	0.011	15.4
~4 μm TiO_2	319.5	7.1	1.55	0.50	0.011	26.8

Figure 6. Electrochemical impedance spectra of the DSSCs fabricated using crystalline Nb_2O_5 nanoporous networks and anatase TiO_2 nanotube arrays. (a) Nyquist plots of the measured and fitted impedance spectra of Nb_2O_5 nanoporous networks and TiO_2 nanotube arrays with thicknesses of ~2 and ~4 μm. They were measured in the dark under the bias voltage of −0.67 and −0.60 V for Nb_2O_5 and TiO_2, respectively, using a CHI 700 electrochemical workstation with impedance analyzer in a two-electrode configuration. A 10 mV AC perturbation was applied ranging between 100 kHz and 10 mHz. (b) Detailed impedance spectra of the marked region shown in panel a. (c) Their corresponding Bode phase plots of measured and fitted impedance spectra. (d) Summary of parametric analysis of the impedance spectra.

chemical stability of Nb_2O_5.[18] However, it is widely known that the major drawbacks for utilizing nanoarchitectures, especially those that are based on nanoparticles, are the increase in the random diffusion of electrons (which leads to a higher likelihood of electron entrapment) and the increase in grain boundary density (which gives rise to defect states in the band gap that perform as trap centers for the free electrons).[19,29] Hence, these effects can largely degrade the electron transport and recombination kinetics. Although TiO_2 nanotube arrays have been suggested to offset these drawbacks, recent research reveals that the possible fluoride and nitrogen impurities in TiO_2 nanotubes, mainly embedded during anodization, can create additional trap states, which is implied to be the cause for lower electron mobility and shorter electron lifetime.[11] Here our Nb_2O_5 nanoporous networks can provide continuous and directional electron transfer pathways, which to a high degree, perform similar to those of TiO_2 nanotube arrays. More importantly, they have much better chemical stabilities, hence minimizing the fluoride and nitrogen doping effect. We find no impurities within these nanoporous networks by utilizing various surface characterization techniques, including XRD, Raman spectroscopy, and X-ray photoelectron spectroscopy (XPS) (detailed XPS spectra of both Nb_2O_5 nanoporous networks and TiO_2 nanotube arrays are provided in Figure S13).

Open circuit voltage decay (OCVD) measurements were performed to estimate effective electron lifetime and verify the above assumptions. According to Figure 5c,d, electrons in these Nb_2O_5 nanoporous networks exhibit much longer effective lifetimes in comparison to those in TiO_2 nanotube arrays, indicating a combined effect of higher energy level of conduction band of Nb_2O_5 and fewer recombination centers in the nanoporous networks.[15,29,34] We further analyzed the electron transport and recombination properties in the photoanodes of Nb_2O_5 nanoporous networks and TiO_2 nanotube arrays by utilizing electrochemical impedance spectroscopy (EIS). EIS is regarded as a powerful technique to characterize the transport and recombination in DSSCs, and appropriate physical models have been developed to interpret the results.[35−37] EIS spectra of Nb_2O_5 and TiO_2 were measured in the dark under the bias voltage of −0.67 and −0.60 V, respectively. A well-developed equivalent circuit by Juan *et al.*[35] was employed to fit the experimental data of impedance spectra for extracting parameters of DSSCs related to electron transport and recombination, using the electrochemical workstation in-built simulation software. Among several key parameters involved in this equivalent circuit, three fitted parameters, which are electron

transport resistance (R_w) in the oxide layer, charge transfer resistance of the charge recombination between electrons in the oxide and I_3^- ions in the electrolyte (R_k), and chemical capacitance of the oxide layer (C_μ), could be used in order to determine the parameters for the evaluation of cell performance, such as the electron transport time (τ_d), effective electron lifetime (τ_{eff}), and effective diffusion length (L_{eff}).[38,39]

According to the Nyquist plots of the impedance spectra in Figure 6a,b, it is seen that the radiuses of the semicircles of the Nb_2O_5 nanoporous networks are almost 10-fold larger than those of TiO_2 nanotube arrays of similar thicknesses, which implies that Nb_2O_5 films have much larger charge transfer resistances and, therefore, greatly enhanced electron lifetimes. This conclusion is also supported by both the Bode phase plot displayed in Figure 6c, in which the left frequency peaks of Nb_2O_5 films (centered at around ~0.8 Hz) are more left-shifted as compared to those of TiO_2, as well as the OCVD results shown in Figure 5d. The fitted parameters shown in Figure 6d indicate that the τ_{eff} values of 2 and 4 μm Nb_2O_5 nanoporous networks are 8.31 and 5.71 s, respectively, which are approximately 13- and 11-fold longer than those of TiO_2 nanotube arrays with similar thicknesses. However, their τ_d values are almost 4 times longer than their TiO_2 counterparts, hence leading to smaller electron diffusion rates. This could be possibly due to the lower natural conductivity of Nb_2O_5 itself. Fortunately, their superiorly enhanced effective electron lifetimes compensate the shortfall of smaller electron diffusion rates in the photoanodes, which results in enhanced L_{eff} in comparison to those of TiO_2 nanotube arrays. Additionally, we have conducted complementary transient absorption spectroscopy for electron recombination investigations of our Nb_2O_5 nanoporous network in comparison to TiO_2 nanotube arrays of similar thicknesses. However, no conclusive differences were observed, and the results are not presented in this paper.

CONCLUSION

In conclusion, we have fabricated Nb_2O_5 crisscross nanoporous networks with a thickness up to ~4 μm by using a unique electrochemical anodization method at elevated temperatures that provides an efficient process to obtain porous morphologies. This nanoporous network offers superior dye-loading sites, excellent continuous and directional pathways for electron transfer, as well as enhanced effective electron lifetimes. These advantages, together with the relatively wider band gap and high conduction band edge of Nb_2O_5, result in an ideal material for the creation of photoanodes for highly efficient DSSC applications. Demonstrated conversion efficiency of 4.1% from a ~4 μm thick Nb_2O_5 photoanode is >50% higher than that of a TiO_2 nanotube array with a similar thickness. The 4.1% efficiency achieved is lower than the 15% value which justifies commercialization but creates real research and development opportunities to enhance performance by synthesizing thicker porous structures as well as utilizing front-side illumination by realizing these structures on transparent conductive substrates.

METHODS

Fabrication of Nanoporous Niobium Pentoxide. The starting material was niobium foil (99.95% purity, Sigma Aldrich) with a thickness of 0.25 mm. The surface of each specimen was cleaned ultrasonically with acetone, then washed with isopropyl alcohol and distilled water, and finally dried in a stream of compressed dry nitrogen. Electrolytes consisting of 50 mL of ethylene glycol (98% anhydrous, Sigma Aldrich) with 0.15–0.50 g of NH_4F (98% purity, Sigma Aldrich) and 0–8 vol % water were initially conditioned by applying 5–20 V between a platinum cathode and a niobium anode. The electrolytes were kept at a constant temperature of 20, 50, or 80 °C during each experiment. Anodization durations of 0.5–4.0 h resulted in films comprising 1.5–6.0 μm thick nanoporous structures. After anodization, the samples were carefully washed with distilled water and dried in a nitrogen stream. After anodization, the sample was annealed in air at a temperature of 440 °C for 20 min, with a slow ramp up and down rate of 1 °C/min.

Structural Characterization. The instruments used were a FEI Nova NanoSEM for SEM; a JEM-3010 300 kV for cross-sectional TEM; and a Bruker D8 DISCOVER microdiffractometer fitted with a general area detector diffraction system (GADDS) for X-ray diffraction. HRTEM samples were prepared by using a cleaned razor blade to scrape the nanostructures onto a holey carbon (Formvar) grid, allowing the surface tension of the grid to hold the nanostructures in place. The HRTEM images were taken using a JEOL2100F HRTEM operating at 200 kV. EDX measurements were carried out on the FEI Nova NanoSEM. Raman measurements were performed using a system incorporating an Ocean Optics QE 6500 spectrometer, a 532 nm 40 mW laser as the excitation source and a notch filter used to prevent measurements below 100 cm^{-1}. XPS measurements were performed on a VG-310F instrument using Al non-monochromated X-rays (20 kV, 15 mA) with the hemispherical energy analyzer set at a pass energy of 100 eV for the survey spectrum and 20 eV for the peak scans.

Solar Cell Fabrication. The Nb_2O_5 electrode was first immersed in a 0.2 mM N3 dye (Solaronix) in a mixture of acetonitrile and *tert*-butyl alcohol (volume ratio 1:1) and kept at room temperature for 24 h. The counter electrode was 30 nm thick platinum, sputtered on a FTO substrate (Delta Technologies). The electrolyte was a solution of 0.6 M 1-butyl-3-methylimidazolium iodide (Sigma Aldrich), 0.03 M I_2 (Sigma Aldrich), 0.10 M guanidinium thiocyanate (Sigma Aldrich), and 0.5 M 4-*tert*-butyl pyridine (Sigma Aldrich) in a mixture of acetonitrile and valeronitrile (volume ratio, 85:15). The dye-adsorbed Nb_2O_5 photoanodes and platinum counter electrodes were assembled into a sandwich-type cell and sealed with a hot-melt sealant with a thickness of 25 μm (Solaronix). The Nb_2O_5 electrodes had dimensions of 5 mm × 5 mm (*i.e.*, 0.25 cm^2).

Solar Cell Characterization. Photovoltaic measurements were performed using an AM 1.5 solar simulator (Photo Emission Tech.). The power of the simulated light was calibrated to 100 mW cm^{-2} by using a reference silicon photodiode with a power meter (1835-C, Newport) and a reference silicon solar cell to reduce the mismatch between the simulated light and AM 1.5.

Current−voltage (*I*−*V*) curves were obtained by applying an external bias to the cell and measuring the generated photocurrent with a Keithley model 2400 digital source meter. The voltage step and delay time of photocurrent were 10 mV and 40 ms, respectively. DSSCs fabricated using commercially available TiO_2 nanoparticle-coated glass plates (Dyesol, Australia) were tested and compared with their factory specifications in order to standardize the cell fabrication and testing conditions. The IPCE values for the cells were determined using a system comprising a monochromator (Cornerstone 330), a 300 W xenon arc lamp, a calibrated silicon photodetector, and a power meter. To establish the dye loading of the sensitized Nb_2O_5 nanoporous networks and TiO_2 nanotube arrays, samples sensitized with N3 were placed into a 10 mM solution of KOH to desorb the dye. Absorbance spectra of the desorbed dye were examined using a spectrophotometric system consisting of a Micropack DH-2000 UV−vis−NIR light source and an Oceanoptics HR4000 spectrophotometer. EIS spectra were measured in the dark under different bias voltages using a CHI 700 electrochemical workstation with impedance analyzer in a two-electrode configuration. A 10 mV AC perturbation was applied ranging between 100 kHz and 10 mHz.

Conflict of Interest: The authors declare no competing financial interest.

Acknowledgment. S.S. and M.B. acknowledge the Australian Post-Doctoral Fellowships from the Australian Research Council through Discovery Projects DP110100262 and DP1092717, respectively. The authors acknowledge the Australian Research Council for equipment funding through the Linkage, Infrastructure, Equipment, and Facilities Grants LE0775679 and LE0989615.

Supporting Information Available: More SEM images of Nb_2O_5 nanoporous networks under different fabrication conditions, cross-sectional TEM image of Nb_2O_5 nanoporous networks, detailed analysis of XRD spectra of Nb_2O_5 porous layers before and after annealing, fabrication details of TiO_2 nanotube arrays, digital images of Nb_2O_5 sample after dye loading and XPS spectra of both Nb_2O_5 and TiO_2 samples. This material is available free of charge *via* the Internet at http://pubs.acs.org.

REFERENCES AND NOTES

1. Kang, T. S.; Smith, A. P.; Taylor, B. E.; Durstock, M. F. Fabrication of Highly-Ordered TiO_2 Nanotube Arrays and Their Use in Dye-Sensitized Solar Cells. *Nano Lett.* **2009**, *9*, 601–606.
2. Mor, G. K.; Shankar, K.; Paulose, M.; Varghese, O. K.; Grimes, C. A. Use of Highly-Ordered TiO_2 Nanotube Arrays in Dye-Sensitized Solar Cells. *Nano Lett.* **2006**, *6*, 215–218.
3. Varghese, O. K.; Paulose, M.; Grimes, C. A. Long Vertically Aligned Titania Nanotubes on Transparent Conducting Oxide for Highly Efficient Solar Cells. *Nat. Nanotechnol.* **2009**, *4*, 592–597.
4. Dang, X. N.; Yi, H. J.; Ham, M. H.; Qi, J. F.; Yun, D. S.; Ladewski, R.; Strano, M. S.; Hammond, P. T.; Belcher, A. M. Virus-Templated Self-Assembled Single-Walled Carbon Nanotubes for Highly Efficient Electron Collection in Photovoltaic Devices. *Nat. Nanotechnol.* **2011**, *6*, 377–384.
5. Durr, M.; Schmid, A.; Obermaier, M.; Rosselli, S.; Yasuda, A.; Nelles, G. Low-Temperature Fabrication of Dye-Sensitized Solar Cells by Transfer of Composite Porous Layers. *Nat. Mater.* **2005**, *4*, 607–611.
6. Kim, Y. J.; Lee, Y. H.; Lee, M. H.; Kim, H. J.; Pan, J. H.; Lim, G. I.; Choi, Y. S.; Kim, K.; Park, N. G.; Lee, C.; *et al.* Formation of Efficient Dye-Sensitized Solar Cells by Introducing an Interfacial Layer of Long-Range Ordered Mesoporous TiO_2 Thin Film. *Langmuir* **2008**, *24*, 13225–13230.
7. Lu, X. J.; Mou, X. L.; Wu, J. J.; Zhang, D. W.; Zhang, L. L.; Huang, F. Q.; Xu, F. F.; Huang, S. M. Improved-Performance Dye-Sensitized Solar Cells Using Nb-Doped TiO_2 Electrodes: Efficient Electron Injection and Transfer. *Adv. Funct. Mater.* **2010**, *20*, 509–515.
8. Gratzel, M. Photoelectrochemical Cells. *Nature* **2001**, *414*, 338–344.
9. Gratzel, M. Recent Advances in Sensitized Mesoscopic Solar Cells. *Acc. Chem. Res.* **2009**, *42*, 1788–1798.
10. Oregan, B.; Gratzel, M. A Low-Cost, High-Efficiency Solar-Cell Based on Dye-Sensitized Colloidal TiO_2 Films. *Nature* **1991**, *353*, 737–740.
11. Richter, C.; Schmuttenmaer, C. A. Exciton-Like Trap States Limit Electron Mobility in TiO_2 Nanotubes. *Nat. Nanotechnol* **2010**, *5*, 769–772.
12. Lin, C. Y.; Lai, Y. H.; Chen, H. W.; Chen, J. G.; Kung, C. W.; Vittal, R.; Ho, K. C. Highly Efficient Dye-Sensitized Solar Cell with a ZnO Nanosheet-Based Photoanode. *Energy Environ. Sci.* **2011**, *4*, 3448–3455.
13. Zheng, H. D.; Ou, J. Z.; Strano, M. S.; Kaner, R. B.; Mitchell, A.; Kalantar-Zadeh, K. Nanostructured Tungsten Oxide—Properties, Synthesis, and Applications. *Adv. Funct. Mater.* **2011**, *21*, 2175–2196.
14. Zheng, H. D.; Tachibana, Y.; Kalantar-zadeh, K. Dye-Sensitized Solar Cells Based on WO_3. *Langmuir* **2010**, *26*, 19148–19152.
15. Le Viet, A.; Jose, R.; Reddy, M. V.; Chowdari, B. V. R.; Ramakrishna, S. Nb_2O_5 Photoelectrodes for Dye-Sensitized Solar Cells: Choice of the Polymorph. *J. Phys. Chem. C* **2010**, *114*, 21795–21800.
16. Sayama, K.; Sugihara, H.; Arakawa, H. Photoelectrochemical Properties of a Porous Nb_2O_5 Electrode Sensitized by a Ruthenium Dye. *Chem. Mater.* **1998**, *10*, 3825–3832.
17. Barea, E.; Xu, X. Q.; Gonzalez-Pedro, V.; Ripolles-Sanchis, T.; Fabregat-Santiago, F.; Bisquert, J. Origin of Efficiency Enhancement in Nb_2O_5 Coated Titanium Dioxide Nanorod Based Dye Sensitized Solar Cells. *Energy Environ. Sci.* **2011**, *4*, 3414–3419.
18. Thavasi, V.; Renugopalakrishnan, V.; Jose, R.; Ramakrishna, S. Controlled Electron Injection and Transport at Materials Interfaces in Dye Sensitized Solar Cells. *Mater. Sci. Eng., R* **2009**, *63*, 81–99.
19. Jose, R.; Thavasi, V.; Ramakrishna, S. Metal Oxides for Dye-Sensitized Solar Cells. *J. Am. Ceram. Soc.* **2009**, *92*, 289–301.
20. Wei, M. D.; Qi, Z. M.; Ichihara, M.; Zhou, H. S. Synthesis of Single-Crystal Niobium Pentoxide Nanobelts. *Acta Mater.* **2008**, *56*, 2488–2494.
21. Choi, J.; Lim, J. H.; Lee, J.; Kim, K. J. Porous Niobium Oxide Films Prepared by Anodization-Annealing-Anodization. *Nanotechnology* **2007**, *18*, 055603.
22. Sieber, I.; Hildebrand, H.; Friedrich, A.; Schmuki, P. Formation of Self-Organized Niobium Porous Oxide on Niobium. *Electrochem. Commun.* **2005**, *7*, 97–100.
23. Paulose, M.; Shankar, K.; Yoriya, S.; Prakasam, H. E.; Varghese, O. K.; Mor, G. K.; Latempa, T. A.; Fitzgerald, A.; Grimes, C. A. Anodic Growth of Highly Ordered TiO_2 Nanotube Arrays to 134 μm in Length. *J. Phys. Chem. B* **2006**, *110*, 16179–16184.
24. Karlinsey, R. L. Preparation of Self-Organized Niobium Oxide Microstructures *via* Potentiostatic Anodization. *Electrochem. Commun.* **2005**, *7*, 1190–1194.
25. Mor, G. K.; Shankar, K.; Paulose, M.; Varghese, O. K.; Grimes, C. A. Enhanced Photocleavage of Water Using Titania Nanotube Arrays. *Nano Lett.* **2005**, *5*, 191–195.
26. Sadek, A. Z.; Zheng, H. D.; Breedon, M.; Bansal, V.; Bhargava, S. K.; Latham, K.; Zhu, J. M.; Yu, L. S.; Hu, Z.; Spizzirri, P. G.; *et al.* High-Temperature Anodized WO_3 Nanoplatelet Films for Photosensitive Devices. *Langmuir* **2009**, *25*, 9545–9551.
27. Ghicov, A.; Schmuki, P. Self-Ordering Electrochemistry: A Review on Growth and Functionality of TiO_2 Nanotubes and Other Self-Aligned MO_x Structures. *Chem. Commun.* **2009**, 2791–2808.
28. Mor, G. K.; Varghese, O. K.; Paulose, M.; Shankar, K.; Grimes, C. A. A Review on Highly Ordered, Vertically Oriented TiO_2 Nanotube Arrays: Fabrication, Material Properties, and Solar Energy Applications. *Sol. Energy Mater. Sol. Cells* **2006**, *90*, 2011–2075.
29. Hamann, T. W.; Jensen, R. A.; Martinson, A. B. F.; Van Ryswyk, H.; Hupp, J. T. Advancing Beyond Current Generation Dye-Sensitized Solar Cells. *Energy Environ. Sci.* **2008**, *1*, 66–78.

30. Jehng, J. M.; Wachs, I. E. Structural Chemistry and Raman Spectra of Niobium Oxides. *Chem. Mater.* **1991**, *3*, 100–107.
31. Weissman, J. G.; Ko, E. I.; Wynblatt, P.; Howe, J. M. High-Resolution Electron Microscopy and Image Simulation of TT-, T-, and H-Niobia and Model Silica-Supported Niobium Surface Oxides. *Chem. Mater.* **1989**, *1*, 187–193.
32. Zhu, K.; Neale, N. R.; Miedaner, A.; Frank, A. J. Enhanced Charge-Collection Efficiencies and Light Scattering in Dye-Sensitized Solar Cells Using Oriented TiO_2 Nanotubes Arrays. *Nano Lett.* **2007**, *7*, 69–74.
33. Ning, Z. J.; Fu, Y.; Tian, H. Improvement of Dye-Sensitized Solar Cells: What We Know and What We Need To Know. *Energy Environ. Sci.* **2010**, *3*, 1170–1181.
34. Wang, H. X.; Liu, M. N.; Zhang, M.; Wang, P.; Miura, H.; Cheng, Y.; Bell, J. Kinetics of Electron Recombination of Dye-Sensitized Solar Cells Based on TiO_2 Nanorod Arrays Sensitized with Different Dyes. *Phys. Chem. Chem. Phys.* **2011**, *13*, 17359–17366.
35. Fabregat-Santiago, F.; Bisquert, J.; Garcia-Belmonte, G.; Boschloo, G.; Hagfeldt, A. Influence of Electrolyte in Transport and Recombination in Dye-Sensitized Solar Cells Studied by Impedance Spectroscopy. *Sol. Energy Mater. Sol. Cells* **2005**, *87*, 117–131.
36. Kern, R.; Sastrawan, R.; Ferber, J.; Stangl, R.; Luther, J. Modeling and Interpretation of Electrical Impedance Spectra of Dye Solar Cells Operated under Open-Circuit Conditions. *Electrochim. Acta* **2002**, *47*, 4213–4225.
37. Wang, Q.; Moser, J. E.; Gratzel, M. Electrochemical Impedance Spectroscopic Analysis of Dye-Sensitized Solar Cells. *J. Phys. Chem. B* **2005**, *109*, 14945–14953.
38. Adachi, M.; Sakamoto, M.; Jiu, J. T.; Ogata, Y.; Isoda, S. Determination of Parameters of Electron Transport in Dye-Sensitized Solar Cells Using Electrochemical Impedance Spectroscopy. *J. Phys. Chem. B* **2006**, *110*, 13872–13880.
39. Mukherjee, K.; Teng, T. H.; Jose, R.; Ramakrishna, S. Electron Transport in Electrospun TiO_2 Nanofiber Dye-Sensitized Solar Cells. *Appl. Phys. Lett.* **2009**, *95*, 012101.